Computer simulations of nonequilibrium structure formation in electrorheological fluids

K. C. Hass
Ford Research Laboratory, SRL MD-3028, Ford Motor Company, Dearborn, Michigan 48121-2053
(Received 14 August 1992)

The temporal evolution of three-dimensional structure in an electrorheological fluid under nonequilibrium, high-field conditions is examined by a computer-simulation method similar to that of Klingenberg, van Swol, and Zukoski [J. Chem. Phys. **91**, 7888 (1989)]. A variety of characteristic real-space properties (e.g., the radial distribution function) and the static structure factor $S(\mathbf{q})$ are monitored during the simulation. The field-induced polarization of particles causes rapid chain formation followed by a kinetic trapping into a complicated gel-like state with no obvious lateral ordering. For all volume fractions considered, the first percolating chain appears at ten times the average time to first contact. Quenching of the gel is nearly complete on an order of magnitude longer time scale. The formation of chains results in the growth and narrowing of Bragg-like peaks in $S(\mathbf{q})$ along the field direction. In the direction perpendicular to the field, the first peak in $S(\mathbf{q})$ also grows and shifts to smaller q.

PACS number(s): 82.70.Dd, 61.20.Ja, 78.20.Dj, 83.70.Hq

I. INTRODUCTION

Since the pioneering work of Winslow [1] it has been known that, upon application of an electric field, the suspended dielectric particles in an electrorheological (ER) fluid align themselves into chains and columns parallel to the field. This structural change is accompanied by a dramatic increase in the apparent viscosity of the suspension [2,3]. The time scales on which these structural and rheological changes occur are important considerations for the design of ER fluid devices [4,5].

Most theoretical models of ER fluid structure have employed the techniques of equilibrium statistical mechanics [6–13]. Above a certain threshold field, this approach predicts complete phase separation with the particles condensing into a body-centered-tetragonal (bct) structure [10–12]. Halsey and Toor [9] have argued that such structure formation occurs in two distinct steps; chains and columns first form on an aggregation time scale t_a followed by a coarsening of the columns on a time scale t_c. The coarsening time is predicted to be independent of field. For the short-time kinetics, Halsey and Toor employ a quasiequilibrium approach that applies only at relatively low fields (just above threshold). Most practical ER devices, on the other hand, would operate in the complementary high-field limit [3] where the initial aggregation process is much faster than the time required to relax to a quasiequilibrium state. In this regime, the aggregation is ballistic in nature (as opposed to diffusive) and the particles are rapidly quenched into local potential minima that develop out of the initial configuration.

The nonequilibrium response at high fields is difficult to treat analytically [14]. Of the few experimental studies that have been reported [5,15–17], the most notable are the recent optical transmittance measurements of Ginder and Elie [17]. These authors observed that in ac fields where electrophoretic effects are unimportant, $t_a \propto E_0^{-2}$, where E_0 is the applied (rms) field. This is what one expects for particles moving in a viscous medium under the influence of field-induced dipolar forces [18]. Additional information on the kinetics of structure formation in high fields is available from computer simulations [19–23]. The most extensive results have been reported for two-dimensional (2D) systems by Klingenberg, van Swol, and Zukoski (KvSZ) [19]. In three dimensions (3D), the initial aggregation process has been examined only peripherally in the simulations of Whittle [21] and Melrose [23]. The results of the latter study are particularly interesting in that they suggest the formation of a quenched gel-like state with no obvious ordering perpendicular to the field.

In this paper, I present a more thorough analysis of the early stages of 3D structure formation in the high-field limit of ER fluids with use of a computer-simulation method similar to that of KvSZ [19]. The key ingredients of this approach are (1) field-induced interparticle forces based on the point-dipole approximation, (2) a hard-core repulsion to prevent particle overlap, and (3) a Stokes drag treatment of the hydrodynamic resistance of the suspending fluid. Although very approximate, this method is believed to capture most of the essential qualitative physics of ER fluids [3]. Equally important for the present study is the computational efficiency of this approach, which allows for extensive configuration averaging. Such extensive averaging is necessary here because the nonequilibrium nature of the high-field response makes it difficult to obtain accurate statistics, particularly for the time evolution of the static structure factor $S(\mathbf{q})$.

The trade-off between accuracy and computational efficiency is always a major concern in computer simulations. Without question, the most accurate simulation method yet developed for ER fluids is that of Bonnecaze and Brady [22], which includes a much more complete treatment of electrostatic and hydrodynamic forces than the present approach. To date, however, that approach has been applied primarily to 2D systems of 25 particles (on a Cray supercomputer). Here, I average over as many as 500–1000 3D realizations of 256 particles (on an IBM workstation).

The organization of this paper is as follows. Section II reviews the computer-simulation method of KvSZ [19] and emphasizes the novel aspects of the present implementation. The temporal evolution of real-space properties (e.g., pair distribution function, cluster size) are presented and discussed in Sec. III. Section IV describes the temporal evolution of $S(\mathbf{q})$, which is the quantity most easily probed by light-scattering experiments. The paper concludes in Sec. V with a few perspective comments.

II. SIMULATION METHOD

An ER fluid is modeled here, as in Ref. [19], as a neutrally buoyant, monodisperse suspension of hard spheres of diameter σ and dielectric constant κ_p in a fluid of dielectric constant κ_f and viscosity η. Both the particles and the fluid are assumed to be nonconducting [24]. Because of the dielectric mismatch, conveniently characterized by the parameter

$$\beta=\frac{\kappa_p-\kappa_f}{\kappa_p+2\kappa_f} , \tag{1}$$

the application of an electric field E_0 induces polarization forces between the particles [25]. In Ref. [19], a set of parallel-plate electrodes giving rise to the field was explicitly included in the simulation. Here I assume that the separation between these electrodes is orders of magnitude larger than σ (as it would be in most applications) and I concentrate on the bulk response where particle-electrode interactions are negligible. What this means in practical terms is that I consider a simulation cell with periodic boundary conditions in all three dimensions, instead of having two conducting boundaries as in Ref. [19].

The motion of particle i is described in the KvSZ method [19] by Newton's equation of motion

$$m\frac{d^2\mathbf{R}_i}{dt^2}=\sum_{j\,(\neq i)}\mathbf{F}_{ij}-3\pi\eta\sigma\frac{d\mathbf{R}_i}{dt} . \tag{2}$$

Here $\mathbf{R}_i$ is the position of the particle at time t, the first term on the right is the force due to other particles, and the second term is the Stokes drag effect of the intervening fluid. The force on particle i due to the jth particle, separated by a distance R_{ij} in the direction $\hat{\mathbf{e}}_r$, is assumed to be of the form

$$\mathbf{F}_{ij}=F_0\left[\frac{\sigma}{R_{ij}}\right]^4[(3\cos^2\theta_{ij}-1)\hat{\mathbf{e}}_r+(\sin 2\theta_{ij})\hat{\mathbf{e}}_\theta] -F_0e^{-100(R_{ij}-\sigma)/\sigma}\hat{\mathbf{e}}_r . \tag{3}$$

The first term in Eq. (3) is the polarization force calculated for point dipoles with local field corrections neglected; the second term is an effective hard-core repulsion. The dipole-dipole interaction is anisotropic in nature with θ_{ij} the angle between $\hat{\mathbf{e}}_r$ and the field; $\hat{\mathbf{e}}_\theta$ is a unit vector perpendicular to $\hat{\mathbf{e}}_r$, defined previously in Fig. 1 of Ref. [19]. The magnitudes of both interactions in Eq. (3) are scaled by the dipole force,

$$F_0=\tfrac{3}{16}\pi\epsilon_0\kappa_f\sigma^2\beta^2E_0^2 , \tag{4}$$

where ϵ_0 is the permittivity of free space, for convenience.

The limitations of the above model are by now well known [26]. The assumed dipole interaction is only quantitatively reliable for $\beta\ll 1$ or for particles far from contact. Corrections due to many-particle enhancements and multipole effects have been shown to increase the electrostatic forces in some cases by over an order of magnitude [7,24,26–28]. The response times in the present simulations are thus most likely overestimated. The structures that develop, however, are expected to be qualitatively correct since these are determined primarily by the anisotropy of the interactions far from contact, which is unchanged by these corrections. The Stokes drag treatment of hydrodynamic resistance in Eq. (2) is also quantitatively unreliable except in the most dilute suspensions [22,29]. For the volume fractions of interest here ($\phi=0.15$–0.4), many-particle hydrodynamic interactions and lubrication forces may also be significant. As alluded to in the Introduction, the main justification for the neglect of such complicated hydrodynamic and electrostatic effects in the present work is that they would be too costly in terms of computer time. A further limitation of Eq. (3) is the rather arbitrary repulsive force chosen to prevent particle overlap. The steep exponential is about as close to an ideal hard-core interaction as one can include in a simulation without requiring a complicated algorithm for integrating the equations of motion. KvSZ showed [19] that a much softer repulsion tends to produce only isolated chains of particles, which is contrary to what is observed experimentally [15]. Of course, a hard-core repulsion is only a caricature of the short-range interactions in real ER fluids, which are undoubtedly strongly dependent on the choice of materials [3].

Equation (2) also neglects the Brownian forces that result from the thermal motion of molecules in the suspending fluid. These forces are on the order of kT/σ and are responsible for the diffusive aggregation of particles at low fields [9]. The high-field limit of interest here is defined by the condition that $F_0\gg kT/\sigma$. This inequality is very well satisfied in the majority of cases of practical interest [3]. The neglect of Brownian effects is thus an excellent approximation in this limit since particle motion is overwhelmingly dominated by polarization forces.

The simplicity of the present model allows for a convenient transformation to dimensionless variables (denoted by asterisks). Scaling all distances and forces by σ and F_0, respectively, yields $\mathbf{r}_i^*=\mathbf{R}_i/\sigma$ and $\mathbf{f}_{ij}^*=\mathbf{F}_{ij}/F_0$. The natural time unit, first introduced in Ref. [19], is

$$\tau=\frac{3\pi\eta\sigma^2}{F_0}=\frac{16\eta}{\epsilon_0\kappa_f\beta^2E_0^2} . \tag{5}$$

This is essentially the time it takes a particle to move a distance σ while subjected to a constant force F_0. Since all characteristic times in the present simulations are proportional to τ, Eq. (5) describes how such times are affected by various parameters. The E_0^{-2} scaling observed in the optical transmittance measurements of Ginder and Elie [17], for example, follows immediately

from this expression. Absolute time units may be obtained by rewriting Eq. (5) in the form

$$\tau(\text{sec}) = \frac{1.81\eta(\text{Pa sec})}{\kappa_f \beta^2 [E_0(\text{kV/mm})]^2} . \quad (6)$$

For the typical values [3] $\kappa_f = 2$, $\beta = 0.5$, $\eta = 0.1$ Pa sec, and $E_0 = 1$ kV/mm, Eq. (6) yields $\tau = 0.36$ sec. In terms of $\mathbf{r}_i^*$, $\mathbf{f}_{ij}^*$, and $t^* = t/\tau$, Eq. (2) may be written as

$$\left[\frac{m\sigma}{F_0\tau^2}\right] \frac{d^2\mathbf{r}_i^*}{d(t^*)^2} = \sum_{j\,(\neq i)} \mathbf{f}_{ij}^* - \frac{d\mathbf{r}_i^*}{dt^*} . \quad (7)$$

For most realistic parameters (e.g., the above, together with $\sigma = 1$ μm and $m = 10^{-12}$ kg), the quantity in square brackets in Eq. (7) is vanishingly small ($\sim 10^{-6}$). This indicates that particle motion is strongly damped and that inertial effects may be safely neglected. The present simulations, like those of KvSZ [19], are thus based on the simple first-order equation of motion

$$\frac{d\mathbf{r}_i^*}{dt^*} = \sum_{j\,(\neq i)} \mathbf{f}_{ij}^* . \quad (8)$$

The simulation cell here is chosen to be cubic with one axis aligned with the field and periodic boundary conditions. For a cell containing N particles, the length of a side of the cube is chosen to be $L^* = (\pi N/6\phi)^{1/3}$, where ϕ is the desired volume fraction [30]. In most previous ER fluid simulations [19–23], initial configurations in the absence of a field were generated by randomly positioning particles one at a time so that no two particles overlap. This method of "random sequential addition" [31] runs into the well-known "parking problem" [32] at high volume fractions ($\phi > 0.32$) and, even at low volume fractions, produces configurations that differ in subtle ways from those of an equilibrium ensemble for a hard-sphere liquid [31]. To avoid these problems in the present work, I first place the N particles on a face-centered-cubic (fcc) lattice and generate an initial random configuration by letting the system evolve via a Monte Carlo (MC) algorithm [33]. In each MC step, each coordinate of every particle is allowed to change by some random value between $-\delta r^*$ and $+\delta r^*$; the move of any given particle is rejected if it causes particles to overlap and accepted otherwise. The value of δr^* is adjusted every 30 MC steps to keep the probability of acceptance near 30%. The melting of the initial fcc lattice is monitored through the mean-squared displacement per particle and the structure factor for a fcc reciprocal lattice vector. For the volume fractions considered here, I have found that 1000 MC steps is generally sufficient to ensure a random starting configuration. I then generate different starting configurations for the same ϕ by continuing the MC evolution 100 steps at a time.

The starting configuration describes the initial conditions when the field is instantaneously applied at $t^* = 0$. At that time the system begins to evolve according to Eq. (8). This equation is integrated here using Euler's method with a time step $\Delta t^* = (1.0 - 1.25) \times 10^{-3}$. Larger values of Δt^*, although desirable for probing longer time scales, were found to produce prohibitively large forces because of the steep exponential repulsion in Eq. (3).

The choice of N is also a compromise. Since the computer time scales as N^2, it is computationally more efficient to generate good statistics by making many runs at smaller N than a few runs at large N. Too small a value of N, however, greatly limits the length scale on which structural properties can be probed and the resolution with which the structure factor can be determined (cf. Sec. IV). Unless otherwise indicated, the present results were obtained with $N = 256$. Tests performed at larger and smaller N showed no significant differences.

One final consideration is the range of interparticle interactions in Eq. (3). Here, as in most previous simulations [19–21,23], I simply cut off these interactions beyond a separation r_c^*. For most runs with $N = 256$, I use $r_c^* = 3.5$, which is always smaller than L^*. While some properties of ER fluids may well be influenced by the long range of dipolar forces (e.g., the predicted coarsening on long-time scales [9,34]), the present results for the short-term kinetics in high fields are not strongly dependent [35] on the choice of r_c^*.

III. REAL-SPACE PROPERTIES

As an example of the evolution of structure in 3D, I first consider a simulation based on a single realization of 108 particles with $\phi = 0.25$. A complicating factor in 3D is the difficulty in visualizing the results. Figure 1 shows projections of the simulation cell along the field direction with the diameter of the particles (circles) in proper proportion to the cell size. At $t^* = 0$ in Fig. 1(a), the particles are randomly distributed and almost the entire projected area is occluded by at least one particle. Figures 1(b)–1(d) show the same projection at times $t^* = 1$, 10, and 100, respectively. According to Eq. (3), pairs of particles with $\theta_{ij} < 54.7°$ attract each other and those with $\theta_{ij} > 54.7°$ repel. This produces significant particle chaining along the field direction (i.e., perpendicular to the projection), which is already evident by $t^* = 1$. At longer times, the chains become increasingly well aligned due to the lateral motion of the particles. The projected area not blocked by particles increases dramatically from $t^* = 0$ to 100. Figure 2 shows a projection at a still later time ($t^* = 1000$) with the simulation cell repeated periodically in the lateral directions to emphasize the continuity of structure. Only minor changes appear to have occurred between $t^* = 10$ and 1000. If the simulation were extended further, the particles would remain relatively fixed. A longer run is not practical, however, as Fig. 2 already corresponds to 10^6 time steps, each of which requires on the order of 0.1 sec of CPU time for $N = 108$ on the IBM RS/6000 workstation used here.

Figure 3 shows a 3D perspective drawing of the simulation cell for the final structure in Fig. 2. Here the chains are more easily visualized and it is clear that not all "chains" extend across the entire cell and some contain as few as two particles. The chains themselves have aggregated into a complicated gel-like state with each chain typically connected to only two or three others. This state was first identified by Melrose [23] and is found in all of the present simulations. Its existence is a conse-

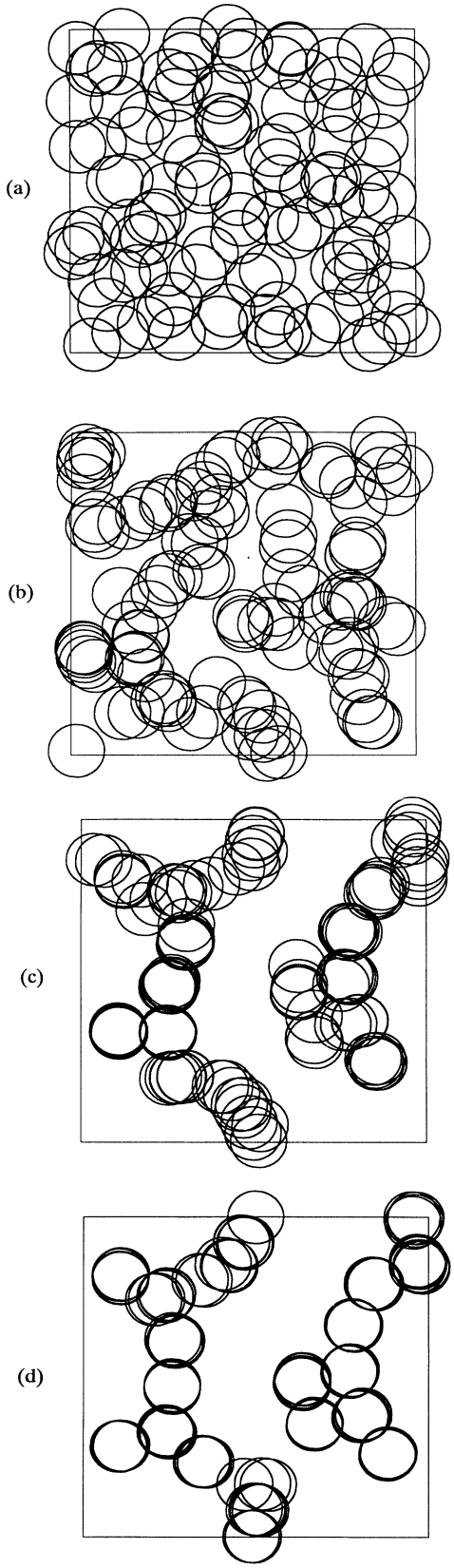

FIG. 1. Projections in a plane perpendicular to the field of a simulation cell containing 108 particles at (a) $t^*=0$, (b) $t^*=1$, (c) $t^*=10$, and (d) $t^*=100$. The volume fraction is 0.25.

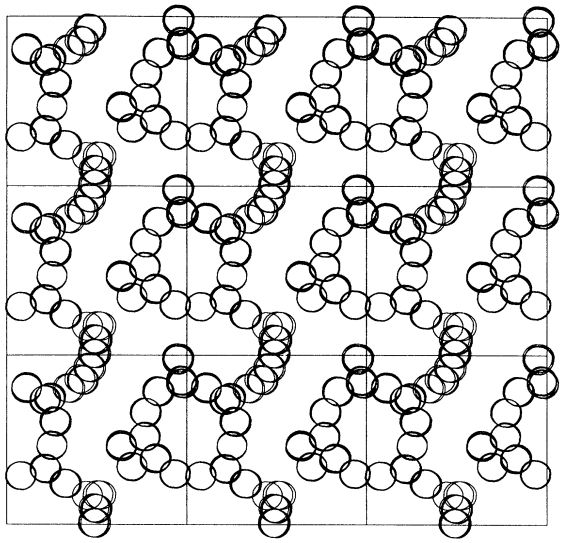

FIG. 2. Projection in a plane perpendicular to the field for the same simulation as in Fig. 1 at $t^*=1000$. The simulation cell is repeated here to emphasize the periodic boundary conditions.

quence of the kinetic trapping at high fields that impedes the formation of the more compact bct lattice structure predicted by equilibrium theory [10–12]. The contact between two neighboring chains in Fig. 3 is similar to that in a bct lattice, but there is no obvious lateral ordering in the gel state.

Figure 1 suggests that the main features of the gel form by $t^*\approx 10$. For the typical ER fluid parameters discussed in Sec. II, this yields a formation time on the order of seconds (or even shorter, given that the present model underestimates polarization forces). Eventually, of course, equilibrium considerations must win out, but it is unclear whether the simple picture of coarsening proposed by

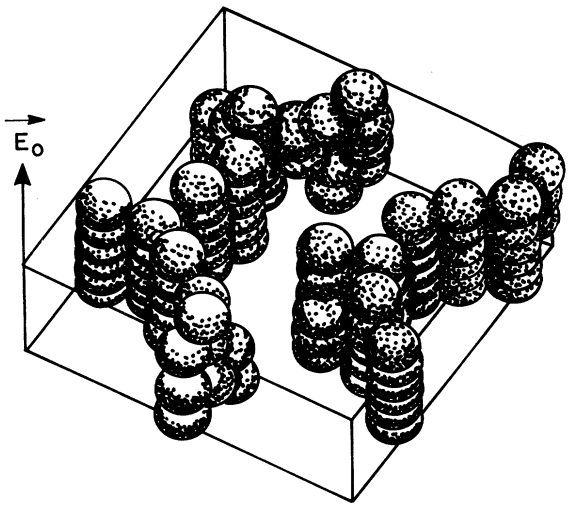

FIG. 3. Three-dimensional perspective drawing of the simulation cell for the $t^*=1000$ structure in Fig. 2.

Halsey and Toor [9] remains valid once the gel has formed. The rapidly formed gel thus most likely dominates the high-field behavior in experiments and devices. While it is unlikely that the resulting shear forces are significantly different than those for isolated chains, a detailed examination of the mechanical properties of the gel would certainly be desirable.

A more quantitative picture of structural evolution is obtained by averaging over many simulations for a given ϕ beginning with different realizations at $t^*=0$. The real-space results discussed in the remainder of this section are based on averages over 50 runs with $N=256$.

Figure 4 shows the calculated radial distribution function [33] (RDF),

$$g_0(r^*)=\frac{\pi}{6\phi N}\sum_i\sum_{j\,(\neq i)}\delta(r^*-r_{ij}^*)\ , \tag{9}$$

for $\phi=0.25$ at $t^*=0$, 1, and 10. The $t^*=0$ result is in excellent agreement with the known equilibrium RDF for a hard-sphere liquid [36] with $\phi=0.25$. (Note that this would not be the case if the initial configurations were generated by random sequential addition [31].) As soon as the field is applied, the main peak in the RDF at $r^*=1$ grows and narrows at a rapid rate. This results from pairs of particles, particularly those with $\theta_{ij}<54.7°$, being attracted toward contact. This same attraction, together with the repulsion between particles with $\theta_{ij}>54.7°$, causes a depletion in the RDF for $1.05<r^*<1.6$. The appearance of peaks at $r^*\approx 2$ and $r^*\approx 3$ in Fig. 4 confirms that chaining has already begun to occur by $t^*=1$. The small peak at $r^*\approx\sqrt{3}$ is caused by a particle trapped in a local potential minimum adjacent to a chain segment; an example is shown in Fig. 5 where particle 5 is separated by $r^*\approx\sqrt{3}$ from particle 2. By $t^*=10$, all of the subsidiary peaks in the RDF have grown considerably, including an additional peak at $r^*\approx\sqrt{7}$. This new peak corresponds to the separation between particles 1 and 5 in Fig. 5.

The anisotropy of the present problem implies that the full pair distribution function $g(\mathbf{r}^*)$ depends on both r^* and the angle θ between $\mathbf{r}^*$ and the field direction. This function may be expanded as

$$g(r^*,\theta)=\sum_{n=0}^{\infty} g_n(r^*)P_n(\cos\theta)\ , \tag{10}$$

where n is even and $P_n(x)$ is the nth-order Legendre polynomial [37]. The $n=0$ term in Eq. (8) is the RDF already considered. In many previous studies of ER fluids [6,7,21], Eq. (10) has been truncated at $n=2$. While this approximation is reasonable in the low-field liquid state [7,13], it is unreliable in the present context. Figure 6 shows an enlargement of the $g_0(r^*)$ results from Fig. 4(b) along with the corresponding quantities $g_2(r^*)$ and $g_4(r^*)$ for $t^*=1$. Even at this relatively short time, $g_4(r^*)$, and higher n terms, are as significant as $g_2(r^*)$. The strong anisotropy associated with the formation of strongly aligned chains is thus poorly described by only the low-order terms in Eq. (10).

The unusual structure in $g_2(r^*)$ and $g_4(r^*)$ near $r^*=1$ in Fig. 6 is a consequence of the slightly softened "hard-core" repulsion in Eq. (3). The zero-force condition in the present model gives a separation between particles along a chain of $r^*=0.993$. The stable position for a particle adjacent to a chain, by contrast, corresponds to the slightly larger separation (e.g., 3–5 in Fig. 5) of $r^*=1.009$. Since θ_{ij} in the former case is close to 0° and in the latter case is close to 60°, the contributions to $g_2(r^*)$ and $g_4(r^*)$ are positive on the low r^* side of the first RDF peak and negative on the high r^* side. The negative regions of $g_2(r^*)$ at larger r^* also represent an excess of particle pairs with $\theta_{ij}>54.7°$. It is these pairs that exhibit the largest relative motion once particles that were initially in close proximity along the field direction have chained up.

Figures 7(a) and 7(b) show the time dependences of the mean-squared displacements of particles in directions perpendicular and parallel to the field, respectively, for $\phi=0.15$ (solid), 0.25 (dashed), and 0.35 (dotted). The results are consistent with previous simulations [19,21] in

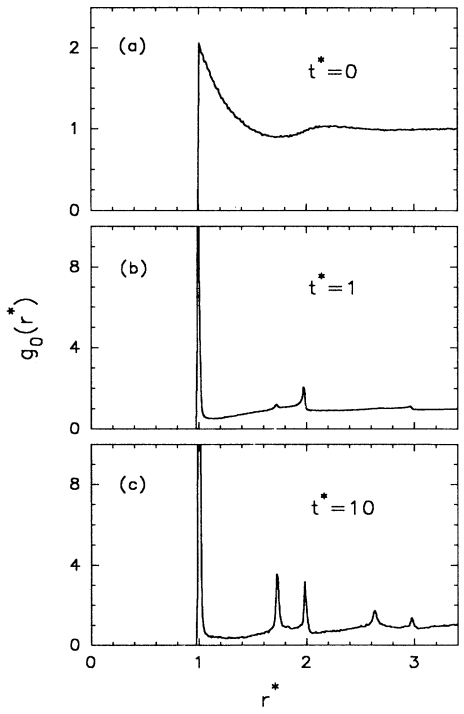

FIG. 4. Radial distribution function for $\phi=0.25$ at (a) $t^*=0$, (b) $t^*=1$, and (c) $t^*=10$.

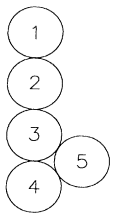

FIG. 5. Typical configuration of particles 1–4 in a chain with particle 5 in an adjacent potential minimum.

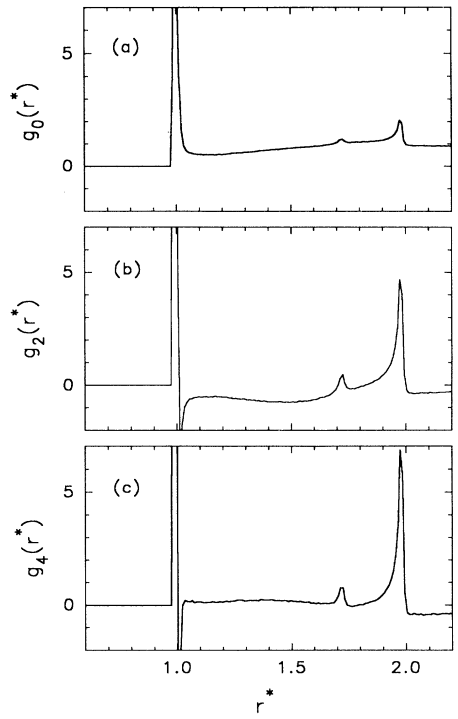

FIG. 6. Components of the full pair distribution function [cf. Eq. (10)] for $\phi=0.25$ at $t^*=1$.

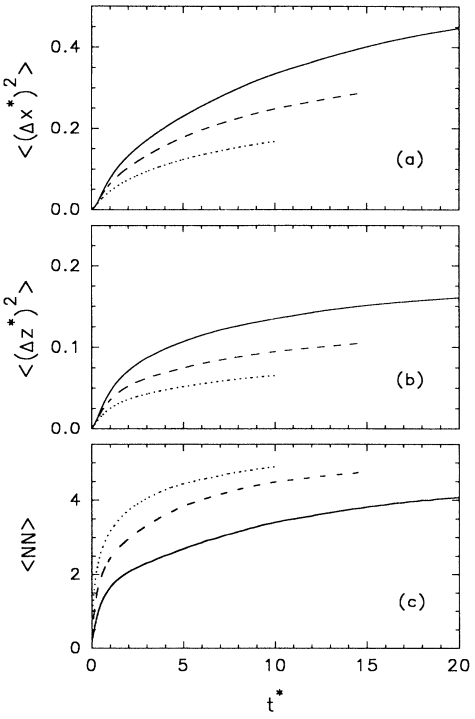

FIG. 7. Time dependences of the mean-squared displacements per particle in the (a) $\hat{\mathbf{x}}$ and (b) $\hat{\mathbf{z}}$ directions, with $\hat{\mathbf{z}}$ along the field, and of the (c) average number of nearest neighbors $\langle NN\rangle$ ($r_{ij}^*<1.03$). The solid, dashed, and dotted curves correspond to $\phi=0.15$, 0.25, and 0.35, respectively.

that they show an initially rapid response followed by a gradual approach to saturation. The mean lateral displacement for a given ϕ is significantly larger than that along the field, but in all cases the total rms displacement is less than a particle diameter. As ϕ increases, the magnitudes of the displacements decrease and the curves level off more rapidly. Both of these effects are to be expected from the smaller average initial separation between particles at larger ϕ. The near saturation of the displacements in Fig. 7 for t^* on the order of 10 is consistent with the lack of substantial changes in structure on longer time scales in Figs. 1 and 2.

Further evidence that the structure is largely quenched by $t^*=10$ is provided by the temporal evolution of the average nearest-neighbor coordination $\langle NN\rangle$ in Fig. 7(c). Nearest neighbors here are defined by the condition that $r_{ij}^*<1.03$, which includes nearly all of the first RDF peaks in Fig. 4. The average coordination approaches saturation even more rapidly than the mean-squared displacements for a given ϕ. For all three ϕ considered, $\langle NN\rangle$ saturates at a value intermediate between that of an isolated chain (2) and that of a 2D triangular (6) or 3D bct (8) lattice. This is another characteristic of the kinetically trapped gel state discussed above. Not surprisingly, the average coordination of the gel increases with ϕ.

Several groups [5,19] have suggested that the onset of the field-induced changes in the rheological properties of an ER fluid is determined by the appearance of the first chain that spans the electrodes. Within the present simulation model, this corresponds to the formation of the first percolating [38] path along the field direction. To identify connected clusters of particles, I have generalized the lattice "multiple labeling algorithm" of Hoshen and Kopelman [39] to the continuum case. As above, I consider particles i and j connected (i.e., nearest neighbors) if $r_{ij}^*<1.03$. Because of the small system size, the time at which the first percolating cluster appears varies greatly from run to run. It is thus convenient to follow KvSZ [19] and monitor the average cluster size [38]

$$S_{\rm av}=\frac{1}{N}\sum_k{}'m_k^2\ , \tag{11}$$

where m_k is the number of particles in the kth cluster and the prime indicates that the sum includes only nonpercolating clusters. Figure 8 shows the temporal evolution of $S_{\rm av}$ for the three volume fractions considered in Fig. 7. The shapes and ϕ dependence of these curves are similar to what had been found previously in the 2D simulations of Ref. [19]. Also consistent with that work, I find that the locations of the peaks in $S_{\rm av}$ correspond very well to the average times at which the first percolating clusters appear [40]. It is thus useful to use the location of the $S_{\rm av}$ peak as a measure of the aggregation time t_a^*, discussed in Sec. I.

The open circles in Fig. 9 show the values calculated from this definition of t_a^* for a range of volume fractions. An alternative measure of t_a^*, shown in the figure as filled

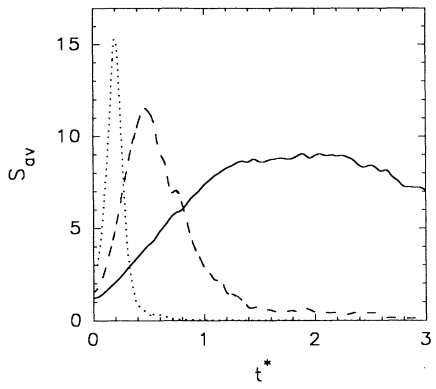

FIG. 8. Time dependences of the average cluster sizes [cf. Eq. (11)] for $\phi=0.15$ (solid), 0.25 (dashed), and 0.35 (dotted).

diamonds, is the time at which $\langle \mathrm{NN} \rangle$ [the quantity in Fig. 7(c), the average number of nearest neighbors] first reaches two. This latter definition is simpler computationally and tracks the location of the maximum in S_{av} remarkably well. The good agreement between these two measures is a consequence of the largely one-dimensional nature of a percolating chain in the present problem. In a more isotropic system, one would generally find a larger average coordination at the onset of percolation [38].

An even shorter characteristic time in ER fluids is the "flocculation" time t_f^*, or average time to first contact. Shapiro, Shalom, and Lin [18] derived analytic expressions for this quantity within a model very similar to that considered here. In the high-field limit, and for nondilute volume fractions, the relevant expression reduces to

$$t_f^* = \frac{1}{40}\left[\left(\frac{\pi}{6\phi}\right)^{5/3} - 1\right] \tag{12}$$

in dimensionless units. (Note that the -1 in the square bracket improves upon the dilute limit expression considered by Ginder and Elie [17].) The solid curve in Fig. 9 shows $10t_f^*$ as a function of ϕ. Remarkably, this curve describes the simulation data for t_a^* extremely well. The characteristic aggregation time, defined by the point at which percolation occurs, may thus be simply estimated as $t_a^* = 10t_f^*$, with t_f^* given by Eq. (12). By contrast, there does not appear to be any theoretical justification for the exponential dependence of t_a^* on ϕ assumed by Hill and Van Steenkiste [5] in their fit to (essentially 2D) experimental data.

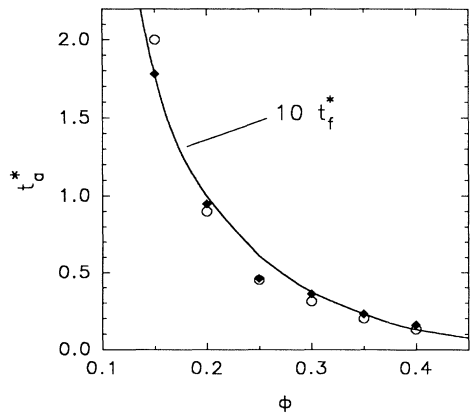

FIG. 9. Volume fraction dependence of the aggregation time t_a^*, defined by either the location of peaks in S_{av} (open circles) or the condition that $\langle \mathrm{NN} \rangle = 2$ (filled diamonds). The solid curve is ten times the flocculation time t_f^* defined in Eq. (12).

The flocculation times given by Eq. (12) are within a factor of 2 of those estimated from the condition that $\langle \mathrm{NN} \rangle = 1$. On still shorter time scales, for the higher volume fractions considered here, $\langle \mathrm{NN} \rangle$ actually dips slightly before increasing. This effect, which is impossible to see on the scale of Fig. 7(c), results from the repulsion between some pairs of particles which are initially close to contact. It is also interesting to note that the mean-squared displacements in Figs. 7(a) and 7(b) initially vary as $(t^*)^2$, up to about $0.5t_f^*$. This behavior may also occur in Fig. 4 of Ref. [19], although it is not mentioned explicitly in that work. In the widely studied case of aggregation dominated by thermal diffusion [41], the mean-squared displacements are expected to increase linearly with t^*. The short-time quadratic increase observed here is most likely a characteristic feature of ballistic aggregation.

It is useful to summarize the temporal evolution of ER fluid structure in high fields as follows. Pairs of particles first come together, or flocculate, on dimensionless time scales of the order of $t_f^* = 0.01-0.2$. The first percolating chain appears at roughly $10t_f^*$. A fully connected gel-like state is almost entirely quenched by $100t_f^*$. Additional minor rearrangements and further connections continue to be made on orders of magnitude longer time scales. Eventually, a complete condensation into a bct lattice [10–12] may occur although it is unclear whether the approach to equilibrium [9] once the gel has formed is ever rapid enough to be of practical concern.

IV. STRUCTURE FACTORS

In principle, light scattering provides one of the most direct probes of the structure of ER fluids and other suspensions [42,43]. Since the particles are usually poorly index matched to the suspending medium, most ER fluids have a milky appearance due to strong multiple scattering. Such strong scattering can either be used to advantage [17], or can be reduced by designing a model fluid with a better index match [43]. In either case, the scattering at any given time is strongly dependent on the static structure factor of the fluid [36],

$$S(\mathbf{q}) = N^{-1}\sum_i \sum_j e^{i\mathbf{q}\cdot(\mathbf{R}_i - \mathbf{R}_j)}, \tag{13}$$

which is a function of the wave vector $\mathbf{q}$. Previously, the behavior of this function in ER fluids had only been addressed for equilibrium conditions [37,44]. The present simulations represent the first treatment of the temporal evolution of $S(\mathbf{q})$ in the nonequilibrium high-field regime.

The static structure factor is closely related [36] to the Fourier transform of the pair distribution function considered in Eq. (10). For the present highly anisotropic case, it is easier, albeit time consuming, to calculate $S(\mathbf{q})$ directly in reciprocal space [45]. First it is convenient to introduce the dimensionless wave vector $\mathbf{q}^*=\mathbf{q}\sigma/2\pi$ and to rewrite Eq. (13) in the more computationally efficient form

$$S(\mathbf{q}^*)=N^{-1}\left[\sum_i \cos(2\pi\mathbf{q}^*\cdot\mathbf{r}_i^*)\right]^2 + N^{-1}\left[\sum_i \sin(2\pi\mathbf{q}^*\cdot\mathbf{r}_i^*)\right]^2 . \quad (14)$$

The periodic boundary conditions imposed in the simulations restrict the allowed wave vectors to the mesh $\mathbf{q}^*=(n_x,n_y,n_z)/L^*$ where n_x, n_y, and n_z are integers. This clarifies the statement at the end of Sec. II that it is the choice of N, and hence L^*, that determines the resolution with which $S(\mathbf{q})$ can be calculated. In the present simulations it is not the resolution that is a problem but the difficulty in obtaining accurate statistics by direct evaluation of $S(\mathbf{q})$. This problem is usually overcome in equilibrium molecular dynamics by extensive time averaging [33] (typically over $>10^3$ time steps). For the dynamical nonequilibrium system studied here, adequate statistics are generated by configuration averaging over 500–1000 runs with different starting configurations. The computational cost of such calculations limits the maximum times considered in this section to t^* on the order of one.

Figure 10 shows $S(\mathbf{q}^*)$ at $t^*=0$ for three different volume fractions. The open and closed circles represent simulation results along the $\hat{\mathbf{x}}$ and $\hat{\mathbf{z}}$ axes, respectively, averaged over 1000 runs with $N=256$. For comparison, the solid curves show the isotropic equilibrium structure factors predicted for hard-sphere fluids by analytic solutions of the Percus-Yevick integral equations [46]. The reliability of this analytic theory for hard spheres has been demonstrated many times previously [36]. That the present simulations agree so well with this theory is testimony to the great care taken in Sec. II to ensure that the random starting configurations are representative of an equilibrium ensemble. Two other things to notice about Fig. 10 are that the spacing between calculated q^* points increases with volume fraction and that the statistical scatter in the results is more pronounced at larger q^* and at smaller ϕ. The first of these follows from the fact that for fixed N, L^* decreases with ϕ. The second reflects the greater difficulty in configuration averaging Eq. (13) for large values of the argument.

For $t^*\neq 0$, $S(\mathbf{q}^*)$ is anisotropic with the same symmetry as Eq. (10). It is sufficient to consider a single quadrant of the plane $\mathbf{q}^*=(q_\perp^*,0,q_\parallel^*)$ with $q_\perp^*,q_\parallel^*\geq 0$ and $\hat{\mathbf{z}}$ the field direction [47]. Figure 11 shows representative plots of $S(q_\perp^*,q_\parallel^*)$ at (a) $t^*=0.5$ and (b) $t^*=1.5$ for $\phi=0.25$. Figure 9 indicates that the shorter of these times corresponds roughly to the percolation point for $\phi=0.25$. Already by this time, significant anisotropies are apparent in $S(\mathbf{q}^*)$, including Bragg-like peaks along

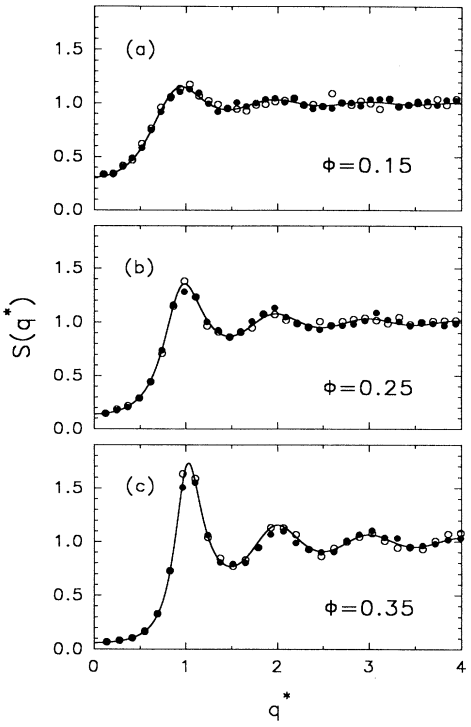

FIG. 10. Open and closed circles represent calculated values of the structure factor $S(q^*)$ for the dimensionless wave vector $q^*=q\sigma/2\pi$ along two orthogonal directions for (a) $\phi=0.15$, (b) $\phi=0.25$, and (c) $\phi=0.35$ at $t^*=0$. Solid curves are analytic predictions for hard-sphere fluids based on the Percus-Yevick approximation.

the field direction at integral values of $q_\parallel^*$. Such peaks are the reciprocal space indicator that chain formation has already begun to occur. By the still longer time considered in Fig. 11(b), the Bragg peaks have become more prominent and the peak in $S(\mathbf{q}^*)$ perpendicular to the field has also grown and shifted to $q_\perp^*<1$. The Bragg peaks fall off only slowly perpendicular to the field due to the absence of any significant lateral ordering in the system. As was the case with the pair distribution function in Eq. (10), the very strong anisotropies in Figs. 11(a) and 11(b) are only poorly described by a truncated expansion in Legendre polynomials.

For emphasis, the $S(\mathbf{q}^*)$ results along the two axes in Fig. 11 are reproduced in Fig. 12 together with the corresponding results for the shorter time $t^*=0.1$. The solid and dashed curves are spline fits to the calculated points parallel and perpendicular to the field, respectively. The Bragg peaks along the field clearly evolve by growing and narrowing continuously out of the initial liquid structure factor. The shift and growth of the first peak in $S(\mathbf{q}^*)$ perpendicular to the field is also striking. The inverse of the location of this peak gives a characteristic measure of the spacing perpendicular to the field, discussed further below. The second peak in the perpendicular direction, near $q^*=1.15$ for $t^*=1.5$, results from the spacing between chains in close contact [48]. The relatively small differences between the two directions at $t^*=0.1$ are

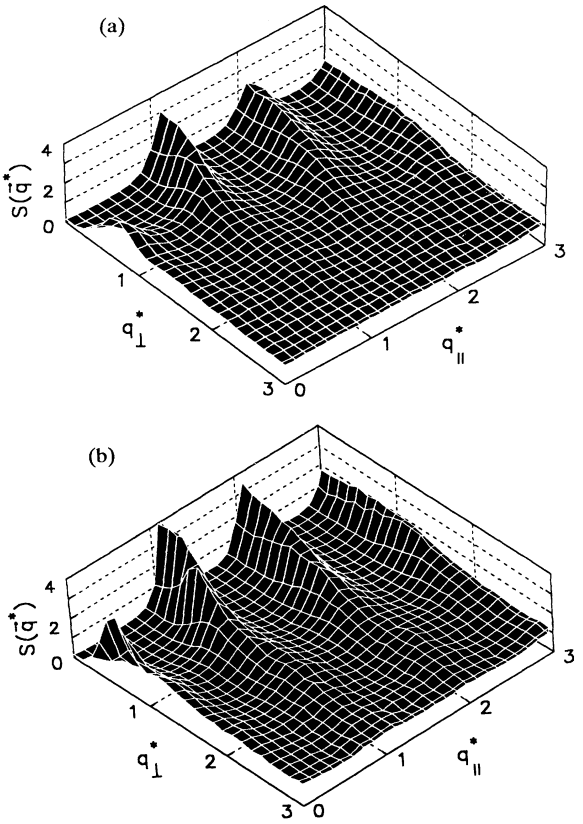

FIG. 11. Three-dimensional plots of the structure factor $S(\mathbf{q}^*)$ in a quadrant bounded by $\mathbf{q}^*$ parallel ($\|$) and perpendicular ($\perp$) to the field direction for $\phi=0.25$ at (a) $t^*=0.5$ and (b) $t^*=1.5$.

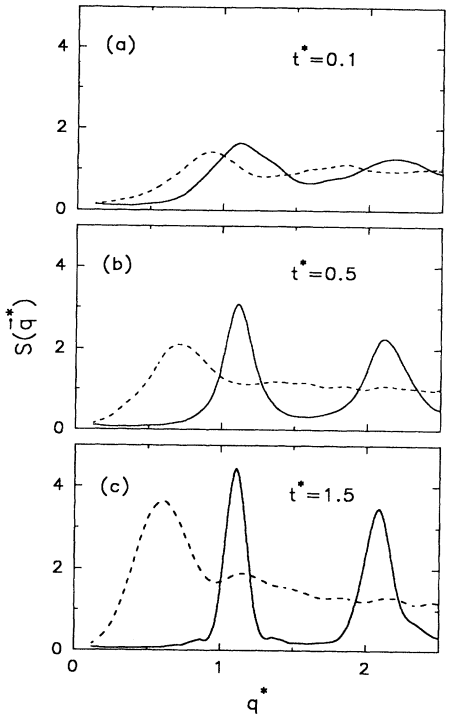

FIG. 12. Calculated structure factors along directions parallel (solid) and perpendicular (dashed) to the field for $\phi=0.25$ at (a) $t^*=0.1$, (b) $t^*=0.5$, and (c) $t^*=1.5$.

reminiscent of the differences predicted for the low-field liquid state of an ER fluid in equilibrium [7,13]. In the high-field case considered here, $S(\mathbf{q}^*)$ is clearly sensitive to the structural changes that occur on very short time scales, even before the first percolating chain appears.

The qualitative features of $S(q_\perp^*, q_\|^*)$ at other volume fractions are similar to those in Fig. 11. A sampling of results along the two principal axes are shown here in Figs. 13 and 14, respectively, for $\phi=0.35$ and 0.15. The main difference between the three cases is that the magnitude of the field-induced changes decreases with increasing volume fraction.

This last statement will now be quantified by examining two characteristic features of the calculated structure factors. The first is the height of the first maximum along the field direction, denoted $S_\|^{\max}$. Figure 15 plots the temporal evolution of this quantity for a number of different runs [35] against the ratio t^*/t_f^* with t_f^* calculated as in Eq. (12). Scaling the time in this manner makes it clear that all of the curves exhibit the same trend. It also shows that the absolute time scale for changes in $S(\mathbf{q}^*)$ varies with ϕ in the same way as the real-space changes in Sec. III. Recall that percolation occurs at $t^*/t_f^* \approx 10$ and that real-space properties saturate at about ten times this ratio, which Fig. 15 suggests will also be the case for $S_\|^{\max}$. The magnitude of the field-induced changes in $S_\|^{\max}$ increases significantly with decreasing volume fraction, as might be expected from the previously observed increase in the magnitude of real-space displacements in Fig. 7.

The second quantity to be extracted from $S(\mathbf{q}^*)$ is the inverse of the $q_\perp^*$ value corresponding to the first peak in the direction perpendicular to the field. This characteris-

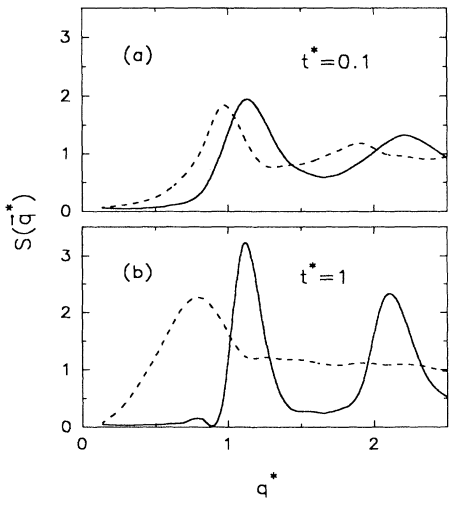

FIG. 13. Same as Fig. 12 but for $\phi=0.35$ at (a) $t^*=0.1$ and (b) $t^*=1.0$.

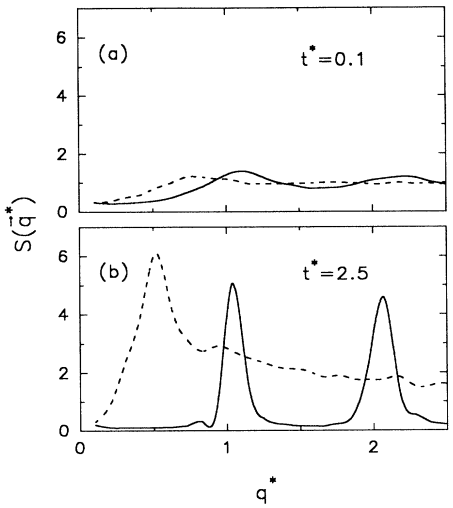

FIG. 14. Same as Fig. 12 but for $\phi=0.15$ at (a) $t^*=0.1$ and (b) $t^*=2.5$.

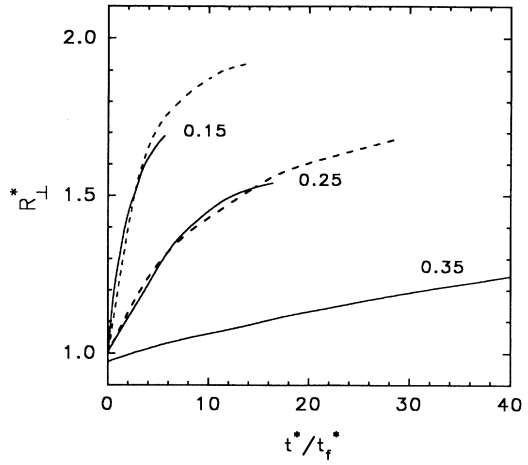

FIG. 16. Characteristic spacing obtained from position of maximum in $S(\mathbf{q})$ for $\mathbf{q}$ perpendicular to the field as a function of t^*/t_f^*, with t_f^* given by Eq. (12). The solid and dashed curves are averages over 1000 and 500 runs, respectively, for the indicated volume fractions. (See also Ref. [35].)

tic lateral spacing $R_\perp^*$ is plotted against t^*/t_f^* in Fig. 16. The qualitative behavior is again similar in each run [35] with the magnitude of the variation increasing with decreasing ϕ. A rough extrapolation from Fig. 16 to the saturation limit suggests that the $R_\perp^*$ corresponding to the $\phi=0.25$ gel state in Fig. 2 is roughly twice the particle diameter. Visually, this appears to be a reasonable measure of the length scale on which the most severe density fluctuations occur in the perpendicular direction. It is important to emphasize that $R_\perp^*$ is not simply a measure of the "width" of "columns" [34]. Chains tend to be more isolated at lower ϕ, as suggested by the coordination number information in Fig. 7(c). A true measure of column width would thus vary with ϕ in the opposite manner from that observed for $R_\perp^*$.

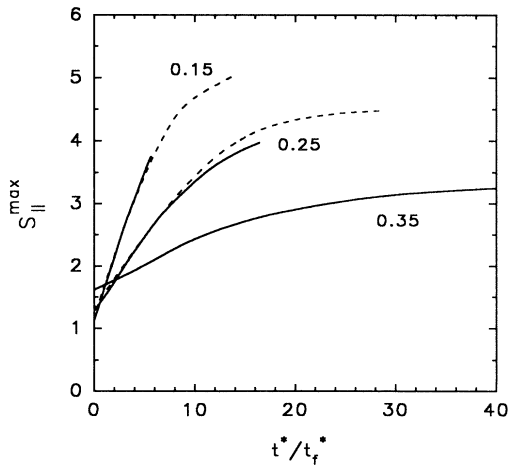

FIG. 15. Maximum value of the structure factor along the direction parallel to the field as a function of t^*/t_f^*, with t_f^* given by Eq. (12). The solid and dashed curves are averages over 1000 and 500 runs, respectively, for the indicated volume fractions. (See also Ref. [35].)

V. CONCLUDING COMMENTS

In summary, I have presented a detailed study of 3D structure formation in ER fluids under nonequilibrium conditions based on the simulation method of KvSZ [19]. The volume fractions considered and the assumed dominance of field-induced polarization forces over thermal effects [3] were motivated by their relevance to practical ER devices. On the longest time scales examined, the particles become kinetically trapped into complicated gel-like states composed of chains parallel to the field with no obvious lateral ordering. Independent of volume fraction, the formation time for this gel is roughly ten times that at which the first chain appears, which is in turn ten times the flocculation time. Evidence of this hierarchy of time scales was obtained from various characteristic measures of structure in real space. In addition, the present work has provided the first extensive predictions for the time dependence of the static structure factor.

It is unfortunate that for the relatively concentrated systems considered there are not yet any sufficiently direct measurements of ER fluid structure with which to compare. The most one can say is that the predicted decrease in the occluded area from Fig. 1(a) to Fig. 1(d) is qualitatively consistent with the previously observed increase [17] in the diffuse optical transmittance through a commercial fluid in a large field. After the completion of this work, a conventional light-scattering study of an index-matched system with $\phi\approx0.05$ was reported [43]. The observed structures are much more anisotropic than any found here, even on time scales as short as a second. The longer time response in these experiments is in qualitative accord with the scenario of column formation and

coarsening proposed by Halsey and Toor [9]. The present study suggests that this scenario breaks down at higher volume fractions due to the rapid quenching of an extended gel-like state. If future experiments prove this to be correct, a more comprehensive examination (including additional computer simulations) of the gel structure and its mechanical properties would be warranted.

ACKNOWLEDGMENTS

I am grateful to L. C. Davis and J. M. Ginder for sharing with me their many insights into ER fluids and for their helpful comments throughout the completion of this work. I have also benefited from conversations with T. C. Halsey, W. G. Madden, and B. C. Xu.

[1] W. Winslow, J. Appl. Phys. **20**, 1137 (1949).
[2] H. Block and J. P. Kelly, J. Phys. D **21**, 1661 (1988).
[3] A. P. Gast and C. F. Zukoski, Adv. Colloid Interface Sci. **30**, 153 (1989).
[4] D. L. Hartsock, R. F. Novak, and G. J. Chaundy, J. Rheol. **35**, 1305 (1991).
[5] J. C. Hill and T. H. Van Steenkiste, J. Appl. Phys. **70**, 1207 (1991).
[6] D. Brooks, J. Goodwin, C. Hjelm, L. Marshall, and C. Zukoski, Colloids Surf. **18**, 293 (1986).
[7] P. M. Adriani and A. P. Gast, Phys. Fluids **31**, 2757 (1988).
[8] R. Tao, J. T. Woestman, and N. K. Jaggi, Appl. Phys. Lett. **55**, 1844 (1989).
[9] T. C. Halsey and W. Toor, Phys. Rev. Lett. **65**, 2820 (1990).
[10] R. Tao and J. M. Sun, Phys. Rev. Lett. **67**, 398 (1991); Phys. Rev. A **44**, 6181 (1991).
[11] W. R. Toor and T. C. Halsey, Phys. Rev. A **45**, 8617 (1992).
[12] L. C. Davis, Phys. Rev. A **46**, 719 (1992).
[13] B. C. Xu and K. C. Hass, J. Chem. Phys. **98**, 2258 (1993).
[14] Some aspects are considered by H. See and M. Doi, J. Phys. Soc. Jpn. **60**, 2778 (1991).
[15] H. Conrad, M. Fisher, and A. F. Sprecher, in *Proceedings of the Second International Conference on Electrorheological Fluids,* edited by J. D. Carlson, A. F. Sprecher, and H. Conrad (Technomic, Lancaster, PA, 1990), p. 63.
[16] T. C. Jordan and M. T. Shaw, in *Proceedings of the Second International Conference in Electrorheological Fluids,* edited by J. D. Carlson, A. F. Sprecher, and H. Conrad (Technomic, Lancaster, PA, 1990), p. 231.
[17] J. M. Ginder and L. Elie, in *Proceedings of the Conference on Electrorheological Fluids,* edited by R. Tao (World Scientific, Singapore, 1992), p. 23.
[18] M. Shapiro, A. L. Shalom, and I. J. Lin, J. Appl. Phys. **58**, 1028 (1985).
[19] D. J. Klingenberg, F. van Swol, and C. F. Zukoski, J. Chem. Phys. **91**, 7888 (1989).
[20] P. Bailey, D. G. Gillies, D. M. Heyes, and L. H. Sutcliffe, Mol. Simulation **4**, 137 (1989).
[21] M. Whittle, J. Non-Newtonian Fluid Mech. **37**, 233 (1990).
[22] R. T. Bonnecaze and J. F. Brady, J. Chem. Phys. **96**, 2183 (1992).
[23] J. R. Melrose, Mol. Phys. **76**, 635 (1992).
[24] For discussions of the effects of finite conductivities in ER fluids, see L. C. Davis, Appl. Phys. Lett. **60**, 319 (1992); J. Appl. Phys. **72**, 1334 (1992).
[25] Under the conditions states, E_0 may be either a dc field or the rms value of an ac field.
[26] D. J. Klingenberg, F. van Swol, and C. F. Zukoski, J. Chem. Phys. **94**, 6170 (1991).
[27] Y. Chen, A. F. Sprecher, and H. Conrad, J. Appl. Phys. **70**, 6796 (1991).
[28] A. M. Kraynik, R. T. Bonnecaze, and J. F. Brady, in *Proceedings of the Conference on Electrorheological Fluids,* edited by R. Tao (World Scientific, Singapore, 1992), p. 59.
[29] J. F. Brady and G. Bossis, Annu. Rev. Fluid Mech. **20**, 111 (1988).
[30] Note that L^* is an integer only for certain discrete values of ϕ. Because of the slightly softened repulsion in Eq. (3), some degree of incommensurability between the simulation cell and a particle chain is to be expected under any circumstances. Larger mismatches must be checked to ensure that they do not make it too difficult for the particles to reach representative bulk configurations. Test simulations over a range of L^* values confirm that the present results are indeed representative.
[31] B. Widom, J. Chem. Phys. **44**, 3888 (1966).
[32] S. Torquato, Appl. Mech. Rev. **44**, 37 (1991).
[33] M. P. Allen and D. J. Tildesley, *Computer Simulation of Liquids* (Clarendon, Oxford, 1989).
[34] W. R. Toor, J. Colloid Interface Sci. **156**, 335 (1993).
[35] The only results presented here with $r_c^* \neq 3.5$ are the dashed curves in Figs. 15 and 16 for which $r_c^* = 4.0$ for $\phi = 0.25$ and $r_c^* = 4.5$ for $\phi = 0.15$. The differences from the $r_c^* = 3.5$ results in these figures and for other properties are small.
[36] J. P. Hansen and I. R. McDonald, *Theory of Simple Liquids* (Academic, New York, 1986), and references therein.
[37] J. B. Hayter and R. Pynn, Phys. Rev. Lett. **49**, 1103 (1982).
[38] For a general discussion of percolation and the significance of S_{av}, see D. Stauffer, *Introduction to Percolation Theory* (Taylor & Francis, London, 1985).
[39] J. Hoshen and R. Kopelman, Phys. Rev. B **14**, 3438 (1976).
[40] As discussed by N. A. Seaton and E. D. Glandt, J. Chem. Phys. **86**, 4668 (1987), the percolation condition must be defined by the properties of the infinite system, not just a single simulation cell. Calculations for N as large as 864 confirm that the present percolation results are not strongly dependent on the cell size.
[41] For a review, see P. Meakin, Annu. Rev. Phys. Chem. **39**, 237 (1988).
[42] Z. Mimouni, G. Bossis, C. Mathis, A. Meunier, and C. Paparoditis, Prog. Colloid Polymer Sci. **81**, 120 (1990).
[43] J. E. Martin, J. Odinek, and T. C. Halsey, Phys. Rev. Lett. **69**, 1524 (1992).
[44] D. R. Nelson, Physica A **177**, 220 (1991).
[45] In isotropic cases, this is usually not true. See, e.g., K. Gaylor, I. Snook, and W. van Megen, J. Chem. Phys. **75**, 682 (1981).
[46] G. P. Montgomery, Jr. and N. A. Vaz, Phys. Rev. A **40**,

6580 (1989).

[47] The extensive averaging over different runs ensures that azimuthal symmetry is restored even if it is broken in individual runs. Azimuthal symmetry breaking would occur, for example, in a bct lattice. The calculated results for the $\hat{\mathbf{x}}$ direction in such a case would represent an average over different lateral orientations. The present results for the parallel direction, however, rule out a significant tendency towards bct ordering; the strong Bragg-like peaks seen here for $q_{\parallel}^{*} \approx 1$ would be suppressed by such ordering due to a destructive interference from the two different types of chains present in the bct structure.

[48] Two chains in contact are separated in the gel, as in a bct lattice, by a dimensionless distance of $\sqrt{3}/2$ perpendicular to the field. The inverse of this corresponds to the peak position at $q^{*} \approx 1.15$.